Journal of the European Ceramic Society 43 (2023) 2740–2751

Contents lists available at ScienceDirect

Journal of the European Ceramic Society

journal homepage: www.elsevier.com/locate/jeurceramsoc

Direct-methane anode-supported solid oxide fuel cells fabricated by aqueous gel-casting

M. Morales [a,b,*], M.A. Laguna-Bercero [c], E. Jiménez-Piqué [a,b]

[a] CIEFMA, Department of Materials Science and Engineering, EEBE, Universitat Politècnica de Catalunya, UPC, C/Eduard Maristany, 10-14, 08019 Barcelona, Spain
[b] Barcelona Research Center in Multiscale Science and Engineering, Universitat Politècnica de Catalunya, UPC, C/Eduard Maristany, 10-14, 08019 Barcelona, Spain
[c] Instituto de Nanociencia y Materiales de Aragón, INMA, CSIC. Universidad de Zaragoza, Pedro Cerbuna 12, 50009 Zaragoza, Spain

ARTICLE INFO

Keywords:
Solid oxide Fuel cell
Aqueous gel-casting
Doped ceria
Methane
Catalytic partial oxidation

ABSTRACT

Direct methane Solid Oxide Fuel Cells (SOFCs) operated under catalytic partial oxidation (CPOX) conditions are investigated, focusing on the processing of the anode support and the anode deactivation caused by carbon deposition. Anode-supported SOFCs based on gadolinium-doped ceria (GDC) electrolyte, and NiO-GDC anode support were fabricated by the gel-casting method. Suitable aqueous slurries formulations of NiO–GDC were prepared, starting NiO-GDC nanocomposite powders, agarose as gelling agent and rice starch as pore former. Electrochemical and mechanical tests evidenced that the support of 550 ± 50 μm thickness and 10 wt% pore former is a good candidate for direct-methane SOFCs. The cells operating under stoichiometric conditions of CPOX reached a performance of 0.64 $W{\cdot}cm^{-2}$ at 650 °C, a very close value to that measured under humidified hydrogen (0.71 $W{\cdot}cm^{-2}$). The best electrochemical stability of the cell is achieved at a CH_4/O_2 ratio of 2.5, showing no evidence of carbon deposition and reducing nickel re-oxidation significantly.

1. Introduction

Solid oxide fuel cells (SOFCs) are electrochemical energy conversion devices which can be used from portable applications of a few watts to megawatt-sized power plants with high efficiency, low emissions of harmful pollution and high flexibility to various fuels [1,2]. Direct methane SOFCs are of special interest, as they present high energy efficiency and relatively simple system design, being an interesting solution for stationary power generation. Methane (CH_4), as the major constituent of natural gas (NG), has attracted considerable attention, due to its relative abundance and its combustion with low emissions of harmful pollutants, such as nitrogen oxides and sulfur dioxide, compared to those of coal and petroleum derivatives [3]. In addition, the use of methane gas in the Power-to-Gas (PtG) technology could play an important role in the energy transition [4,5]. PtG can use renewable or excess electricity to produce hydrogen via steam electrolysis, or syngas (hydrogen and CO mixture) via steam and CO_2 co-electrolysis, which can be used directly as a final energy carrier or converted to different synthetic gases such as methane [6]. However, direct methane SOFCs present a critical issue related to the carbon deactivation of the conventional Ni-electrolyte composite anode, that need to be solved [7].

Complementary strategies such as specific anode materials and microstructures, tuning kinetics and adding oxidant gases, have been developed to address the coking induced anode deactivation during the internal reforming of CH_4. An effective way is the incorporation of gadolinium or samarium doped ceria (SDC or GDC) into Ni-based anodes. It helps to oxidize the carbon species adsorbed on Ni surfaces, due to the excellent oxygen exchange capability of CeO_2 [8]. Doped ceria as an electrolyte can extend the triple phase boundaries (TPBs), due to its oxide-ion conductivity, and also contribute to decrease carbon deposition due to its oxygen storage capacity [9]. The reduction of Ce^{4+} to Ce^{3+} can enhance the catalytic activity and oxygen-exchange processes, but this is resulting in an internal short circuit leading to a decrease of cell performance [10]. This drawback can be attenuated by reducing the operation temperature to about 500–650 °C, or also by the introduction of an electronic blocking layer to avoid the internal short circuit [11].

The state-of-the-art reports several strategies to enhance the Ni-doped ceria anode performance operated on hydrocarbon and oxygenated-hydrocarbon fuels at low temperature. In this sense, the addition of metal promoters, the infiltration or ex-solution of nanoparticles, the insertion of catalyst or functional layers, and the microstructure tuning have been proposed [12,13]. Among them, the

* Corresponding author at: CIEFMA, Department of Materials Science and Engineering, EEBE, Universitat Politècnica de Catalunya, UPC, C/Eduard Maristany, 10-14, 08019 Barcelona, Spain.
E-mail addresses: miguel.morales-comas@upc.edu, mmoralescomas@yahoo.es (M. Morales).

https://doi.org/10.1016/j.jeurceramsoc.2022.06.027
Received 18 February 2022; Received in revised form 30 May 2022; Accepted 7 June 2022
Available online 13 June 2022

microstructure tuning is a promising strategy as a finer-scale microstructure can improve the catalytic properties at lower temperatures. Different methods such as Pechini [14], hydroxide co-precipitation [15], urea-combustion [16], spray pyrolysis [17], and self-assembling [18], have been developed to synthesize NiO–doped ceria anodes with long TPBs and controllable microstructures. Some researchers also concluded that the performance stability can be significantly improved by incorporating small amounts of Mg [19], Sm [20], Sn [21], Ru [22], and W [23], to the nickel-based anode. In addition, the mass transport and length extension of TPBs can promote the electrochemical reactions, and therefore the cell performance, using a hierarchical porous architecture of anode. While the macroporosity improves the gas transport, the meso/micro/nanoporosity increases the active sites for gas adsorption/desorption processes and catalytic reaction. Several techniques for the processing of hierarchical porous architecture anodes have been developed, including the water-storable hierarchical architecture decorated with amorphous BaO and Ni nanoparticles as the anode [24], the silica hard template (KIT-6) combined with a multistep impregnation process to fabricate ordered mesoporous Ni–GDC cermets [25], the hydrothermal method with Pluronic P123 as a template and hexamethylenetetramine as a reducing agent to form macro- and microporosity Ni-SDC anodes [26], and micro- and nanoporosity in Ni-Cu-SDC anodes fabricated by the co-pressing and co-sintering process with ethylcellulose as a pore former [27]. In general, these processing methods present high cost due to long times of forming with many steps, limited number of series, and enormous difficulties to scale-up at the industry. In addition, their development usually requires a long time for the adjustment of processing parameters. An alternative to these laborious methods is the use of conventional techniques such as multilayer and sequential tape-casting [28–30], screen-printing [31,32] and dip-coating [33,34]. They are well-known ceramic processing techniques and offer easy and cheap manufacturing routes, enabling mass production of anode-supported planar solid oxide fuel cells, among others. Another alternative is the gel-casting method that can be also suitable to fabricate porous materials with well controlled porosity [35]. It presents several interesting advantages, as it can be considered as environmentally friendly method, because most of the non-toxic/natural gel-formers can be processed in an aqueous medium. Biopolymers, natural polymers, globular proteins and natural ceramics, such as agar and agarose [36], bovine serum albumin [37], albumen (e.g. egg white) [38], carrageenan [39], curdlan [40], gelatin [41], sodium alginate [42], starch [43], hydratable alumina [44], among others, have been reported as good gel-formers. Furthermore, they are used in extremely low concentrations and they do not require a separate binder removal cycle during firing. With such natural processes, many successful case studies have demonstrated the versatility of this technique towards the development of both fully dense ceramics with simple and complex-shapes, and porous/foamed materials with well controlled porosity features [45–47]. The potential to join dense structures with porous layers, leading to functionally graded ceramics, has been also demonstrated. Moreover, gel-casting processing exhibits a short forming time, high yields and low-cost equipment [48–51]. So, it can be used to shape the fuel cell both in laboratory and at industry scale [52]. Gel-casting as a processing method for microtubular SOFC fabrication has been previously reported [53–56].

In relation with carbon deposition at the anode of SOFCs, it can be inhibited under favourable kinetics and thermodynamics, and defining a suitable operation temperature plays an important role [57,58]. In addition, carbon formation in SOFCs may be also decreased with the flow of oxygen from the electrolyte to anode operating under certain current densities [59]. Therefore, the increase of the current density load can improve the flow of oxygen into the anode, minimizing carbon deposition [9]. However, this flow may only affect the TPBs instead of the whole anode support region [57], and carbon deposition should be avoided in the whole anode [9]. In this sense, higher operation temperatures can thermodynamically shift the condition outside the carbon deposition region as previous studied have demonstrated [58,60]. On the other hand, the addition of the oxidant gases like H_2O, CO_2 and O_2 can also minimize carbon deposition. At the typical SOFC operation temperature (600–1000 °C), Ni can transform CH_4 into syngas via steam reforming of methane (SRM), carbon dioxide reforming of methane (CDRM), catalytic partial oxidation of methane (CPOx) or biomass gasification [61–64]. The most typical internal reforming process is SRM, which uses a mixture of CH_4 and steam that usually fed to the Ni-based anodes, producing syngas as a fuel for the electrochemical oxidation reaction at the anode [10,65]. Nevertheless, coke deposition at the anode deactivates the Ni catalyst, leading to carbon coking inducing catastrophic failure and reducing the operation lifetime of SOFCs [66]. Methane conversion can also be carried out by partial oxidation (Eq. (1) and Eq. (2)), which favours a lower operating temperature, due to its exothermic character [67,68].

$$CH_4 + 1/2\ O_2 \rightleftharpoons 2\ H_2 + CO\ \Delta H^{\circ}(900^{\circ}C) = -23.4\ kJ\ mol^{-1} \quad (1)$$

$$CH_4 + O_2 \rightleftharpoons 2\ H_2 + CO_2\ \Delta H^{\circ}(900^{\circ}C) = -306.3\ kJ\ mol^{-1} \quad (2)$$

A particular case, using the CPOX, to inhibit the coke formation is the use of single-chamber SOFCs (SC-SOFCs) operating with hydrocarbon and air mixtures, exhibiting good power densities at low temperatures [69–71]. However, the H_2 yield and the energy efficiency of the process are relatively low due to the direct oxidation of methane and the low fuel utilization [72]. In the conventional dual-chamber SOFCs, the CPOX on a Ni catalyst can be a good approach to prevent the carbon coking issue and reach a high conversion of CH_4. The easy dissociation of oxygen can help to remove the adsorbed carbon on the Ni surface more effectively than other oxidants like H_2O or CO_2. However, the CPOX approach has rarely been applied to SOFC anodes, as a very low partial pressure of oxygen in the anode chamber should be maintained to develop an electrochemical potential gradient that triggers SOFC operation. In addition, the presence of high concentrations of O_2 into the anode chamber may promote Ni oxidation, and therefore, its catastrophic failure [69]. Despite these issues, some works have demonstrated the optimum microstructures of Ni-YSZ anodes and Ni-doped ceria for the CPOX operating under mixtures of methane and air, obtaining high power densities with stable operation [68,73]. Other studies have reported the critical influence of flow rate and ratio of methane and air on performance stability and coking resistant over Ni-YSZ anodes in SOFCs [74–77].

In the present work, SOFCs fed with methane under CPOX conditions are investigated, focusing on the carbon coking and Ni oxidation as a function of CH_4/O_2 ratio. The presence of oxygen gas in the anode chamber should avoid carbon coking. Ni oxidation can be minimized with oxide ionic conductor based on doped-ceria (GDC), the microstructure tuning using nanocomposite NiO-GDC powders from gel-casting method, and the help of electro- and catalytic reaction controls. Although GDC is more expensive than typical YSZ electrolyte, and therefore, the cost of a SOFC could be increased significantly, the results obtained in this work could be useful to be implemented for downsizing of SOFC designs like microSOFCs, in which the amount of materials is more limited. For this purpose, anode-supported planar cells of NiO–$Gd_{0.2}Ce_{0.8}O_{1.9}$/$Gd_{0.2}Ce_{0.8}O_{1.9}$/$La_{0.6}Sr_{0.4}Co_{0.2}Fe_{0.8}O_{3-\delta}$-$Gd_{0.2}Ce_{0.8}O_{1.9}$ (NiO–GDC/GDC/LSCF-GDC) have been fabricated by a new processing approach. Porous NiO-GDC planar supports have been processed using an environmentally friendly aqueous gel-casting, starting from nanocomposite anode powders synthesized by the sol-gel method. In order to optimize the manufacturing parameters, the formulation of slurries (using water as solvent, rice starch as macropore former and agarose as both gelling agent and sub-micropore former) and the pre-sintering process of planar supports have been investigated. Mechanical strength of cells with different microstructures at the anode support was determined by the 4-point bending method. The Weibull statistical analyses are also presented to understand the reliability on the mechanical properties of the cells. Finally, the electrochemical

characterization of anode-supported planar SOFCs, fabricated by agarose gel-casting method, fueled with several mixtures of methane and air at the anode chamber are reported for the first time. Post-test analysis of cells has been also performed to study the degradation mechanisms during operation.

2. Experimental

2.1. Cell manufacturing

Gadolinium-doped ceria, nickel oxide-gadolinium doped ceria, and lanthanum strontium cobalt ferrite powders, with a nominal composition of $Gd_{0.2}Ce_{0.8}O_{1.9}$, NiO–$Gd_{0.2}Ce_{0.8}O_{1.9}$ (NiO-GDC) and $La_{0.6}Sr_{0.4}Co_{0.2}Fe_{0.8}O_{3-\delta}$ (LSCF), respectively, were synthesized as described elsewhere [51]. The composition of the cells was selected as follows: NiO–GDC (60:40 wt%) as the anode support, NiO-GDC (50:50 wt%) as the anode, GDC as the electrolyte and LSCF-GDC (70:30 wt%) as the cathode. Three anode support types, named as support-0, − 1 and − 2, varying their porosity with 0, 10 and 15 wt% rice starch (Sigma Aldrich), were processed. All the supports presented a thickness around 550 ± 50 μm.

Planar supports were processed by the aqueous gel-casting method, using agarose as gelling agent. Agarose (Sigma Aldrich) and NiO–GDC solids loading were adjusted to achieve a suitable suspension for casting, taking into account that the rheology of the suspensions changed with the added amount of rice starch. According with our previous studies, the explored ranges for the different processing parameters were: NiO–GDC solids loading of 32–44 wt% in distilled water, commercial dispersant (Dolapix GmbH & Co) concentration of 0.6–1.2 wt% with respect to the solids, and agarose content of 0.6–1.1 wt% with respect to the suspension. In order to obtain a homogeneous slurry, the agarose suspension was firstly activated by heating at around 80–90 ºC for 1 h, and then kept above 60 ºC for 1 h until casting in order to avoid premature gelation. During this process, the suspension was degassed under vacuum to remove the air bubbles formed by mixing the ceramic slurry ingredients. The formulation of each studied suspension was adjusted to achieve proper rheological properties, thus improving flow ability and castability. Rheological properties were determined using a rheometer (RST CPS. Brookfield 3000). Viscosity values between 1.0 and 2.0 Pa.s at 60 ºC and a constant shear rate of 100 s^{-1} were established as suitable for casting.

The planar supports were formed using a simple wet-forming technique based on gel-casting, operating as a wet pressing machine with a mold. As shown in the schematic view of Fig. 1, a versatile home-made equipment was used, which present two parts: a ram and die that also acts as a vessel of suspension before and during gelation. The die is filled with the suspension to a determined level, and subsequently the ram presses onto the suspension to a controlled depth with the help of a ring. After several minutes, the suspension is gelled, and the ram can be moved handly, allowing an easy expelling of the body through the end of the die. Both die and ram are made of glass to prevent the formation of surface defects, to keep the required flatness during the gel-casting and drying processes, and to allow an easy removal. The size of die and ram depends on the desired dimensions of the final planar cell, and the depth and shape of the product being made. For instance, cylindrical planar supports between 15 and 40 mm diameter (after sintering) were successfully obtained with this method (Fig. 2).

The resulting green supports were demolded, cut to obtain button cells, and dried under controlled conditions (from 100 % to an ambient relative humidity at room temperature for 10 days) in order to avoid the generation of excessive stress within the support due to differential drying. After that, an anode with a composition of 50:50 wt% NiO–GDC and thickness of 18 ± 2 μm was deposited by colloidal spray-coating onto the planar supports. An ethanol-based ink made of 10 wt% NiO–GDC and 1 wt% of polyvinylpyrrolidone (PVP) as dispersant, was prepared to possess low viscosity, high volatility, and moderate solids loading. In order to optimize the co-sintering process, it was necessary to determine the shrinkage behavior of the different cell components. For this purpose, an estimation was obtained from the shrinkage curves of NiO–GDC supports and a compact pellet of GDC powder prepared from the uniaxial pressing method (100 MPa). The linear shrinkage curves were determined using a dilatometer (LINSEIS L75 PT Horizontal) heating at 1 ºC·min^{-1} up to 1400 ºC. From the results of shrinkage curves, the thermal treatment of the NiO–GDC anode and support were pre-sintered in air. Subsequently, cells were fabricated using previously optimized standard procedures. GDC electrolyte layer was deposited by colloidal spray-coating, ultrasonically mixing GDC powders with terpineol (1:5 wt/wt) and small amounts of cobalt oxide (2.0 wt%) were used as a sintering aid [78]. Previously, GDC powders were ball-milled in ethanol media for more than 6 h at 300 rpm using yttria-stabilized-zirconia jar and balls (5 mm in diameter) to remove the formation of large agglomerates of the synthesized nanopowders. Then, both anode and electrolyte layers were cosintered at 1400 ºC for 5 h. Subsequently, a cathode ink was prepared using 10 wt% LSCF–GDC and 1 wt% PVP in ethanol, which was sprayed onto the half-cell, and finally sintered at 1150 ºC for 2 h in air. Final button cells presented 20 mm diameter, 550 ± 50 μm thickness in total, 500 ± 50 μm thick anode support, 18 ± 1 μm thick electrolyte, and 30 ± 3 μm thick cathode of 1 cm^2 active area.

2.2. Mechanical characterization of supports

Mechanical characterization of the NiO-GDC supports was performed by 4-point bending test, using a universal testing machine (Zwick Roell). For this purpose, specific NiO-GDC supports with cylindrical rod geometry of 50 mm length and 10 mm diameter were processed using the same experimental procedure of the cell supports [51]. The flexural bending strength (σ_{max}) was calculated from the following Eq. (1) [79]:

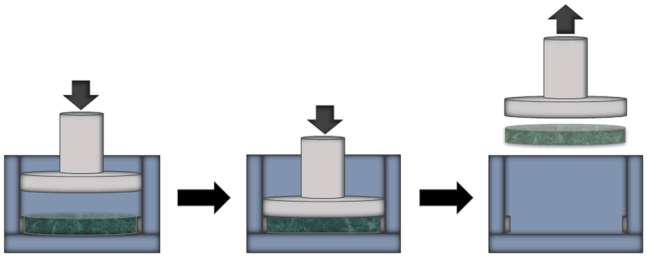

Fig. 1. Schematic illustration of the system device to shape planar supports.

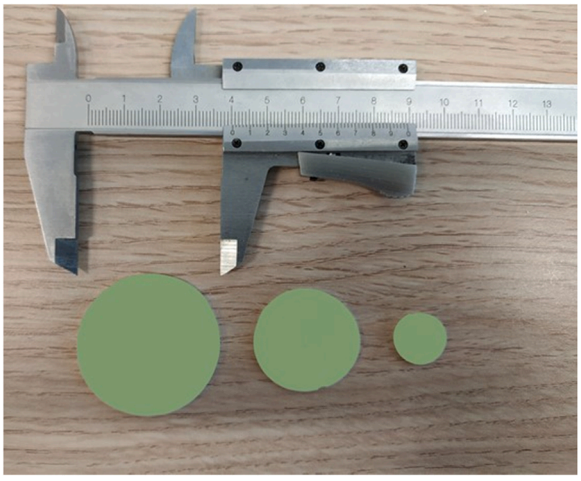

Fig. 2. Planar supports with different dimensions, after sintering process.

$$\sigma_{max} = \frac{8P(L_0 - L_i)}{\pi D^3} \quad (1)$$

where P is the maximum force, L_0 the support span length, L_i the load span length, and R the sample diameter. The measurements were performed according to standard ASTM C1161–02c in air at room temperature [80,81]. Each mechanical value presented for each cell configuration is an average of at least 17 measurements. In order to understand the reliability of the bending strengths, their variability was analyzed using the Weibull statistical method [55,82].

2.3. Electrochemical characterization

Electrochemical characterization of cells was carried out in a commercial ProboStatTM (NorECs AS) sample holder placed inside a high temperature tubular furnace. Gas tightness between the fuel and oxygen chambers was ensured by using Ceramabond 503 (Aremco, USA) ring covering the sample edge. Electrical connections were made using four Pt wires. Pt meshes, and Pt and LSC pastes on surfaces of anode and cathode, respectively, were used as current collectors. Additional details of the experimental setup can be found in previous works [83,84]. The cell was heated to 750 °C inside tubular furnace under nitrogen (100 ml·min^{-1}) at the anode chamber and synthetic air (100 ml·min^{-1}) at the cathode chamber. At this temperature, RT humidified hydrogen (97 % H_2 and 3 % H_2O, 80 ml·min^{-1}) was introduced to reduce the anode. Subsequently, electrochemical measurements were carried out at 650 ºC. Details about fuel composition and flows are specified in the results and discussion section. Polarization current density−voltage curves (j–V) and AC Electrochemical Impedance Spectroscopy (EIS) measurements were recorded using a VSP potentiostat/galvanostat (Princeton Applied Research, Oak Ridge, TN, USA). Polarization curves were performed in galvanostatic mode with a sweeping rate of 20 mA s^{-1}. EIS experiments were conducted at OCV and 0.3 A·cm^{-2} conditions by scanning a frequency range from 1 MHz to 0.1 Hz with an AC signal of 50 mA. Finally, stability tests of the cells were performed in OCV and galvanostatic SOFC mode at a fixed current density of 0.3 A·cm^{-2}, for a complete characterization of the processed cells.

2.4. Complementary characterization

The quality of synthesized powders was characterized by X-ray Powder Diffraction (XRD, Bruker D8 Advance) and Brunauer-Emmett-Teller (BET) determination specific surface (Micrometrics model Tristar 3000). The total porosity of anode supports was determined from the difference between the theoretical and real densities, and using a helium gas absorption pycnometer (Micromeritics ASAP2000) to determine the apparent density. Morphological analysis of the NiO-GDC powders was observed by transmission electron microscopy (TEM, Philips 301). Microstructures of the cells were analyzed by field emission scanning electron microscopy (FE-SEM, Carl Zeiss Auriga) using backscattered electron (BSE), secondary electron (SE) and in-lens secondary electron (IL-SE) detectors. The Ni oxidation in Ni-GDC supports was characterized by X-ray photoelectron spectroscopy (XPS, K-alpha, Thermo Fisher Scientific). The composition of effluent gases, using methane and air as a fuel, was analyzed by online gas chromatography (3000 A microGC, Agilent Technologies) equipped with molecular sieve, a Poraplot, and QV-1 columns, and thermal conductivity detectors (TCD). The TCD signals were calibrated using known flow rates of pure gases (CH_4, H_2, CO, CO_2, and N_2) with N_2 as the internal standard. All GC analyses were performed under a constant total flow rate of the supplied gases.

3. Results and discussion

3.1. Characterization of NiO-GDC nanocomposite powders

Fig. 3a shows the XRD patterns of the as-synthesized NiO-GDC powders used for processing of supports, after calcination at 550 ºC in air. Three intense diffraction peaks corresponding to (111), (200), and (220) lattice planes of the NiO cubic phase are observed [53]. Six lattice planes of (111), (200), (220), (311), (222) and (400) confirm the GDC fluorite structure. The XRD patterns detected no evidence of secondary phases. An anode specific surface of 68 m^2 g^{-1} and a particle size of around 20 nm were obtained by BET technique. Additionally, morphological analysis of the NiO-GDC powders, using TEM, is shown in Fig. 3b. A good homogeneous distribution of faceted grains with a grain size smaller than 40 nm was observed.

3.2. Slurry formulation of supports

Table 1 shows the formulations of NiO-GDC suspensions for the gel-casting system of the different cell supports. Among the explored dispersant amounts, a Dolapix content of 0.9 wt% vs. NiO-GDC powder is suitable for dispersing and stabilizing the powder in distilled water. Dispersant amounts higher and lower than this amount affect negatively the stability of suspension. On the other hand, the viscosity increases moderately with the solids loading content from 32 wt% to 40 wt% (Fig. 4a). When solids loading content exceeds 40 wt%, the viscosity increases sharply. For 42 wt% solids loading, the suspension viscosity

Table 1
Formulations of NiO-GDC suspensions for the gel-casting system of the different cell supports.

Formulation	Solids loading vs. water (wt%)	Dispersant vs. solids loading (wt%)	Rice starch vs. solids loading (wt %)	Agarose vs. suspension (wt %)
0	40	0.9	0	0.8
1	38	0.9	10	0.8
2	36	0.9	15	0.8

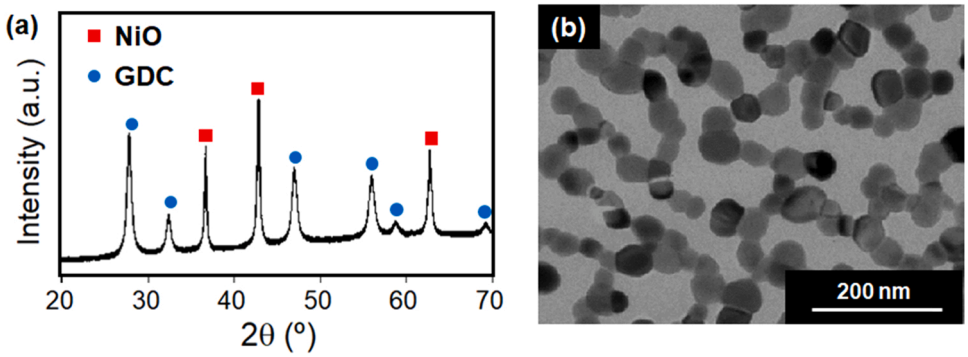

Fig. 3. (a) XRD patterns, and (b) TEM image. of the NiO–GDC nanocomposite powders after calcination at 550 ºC.

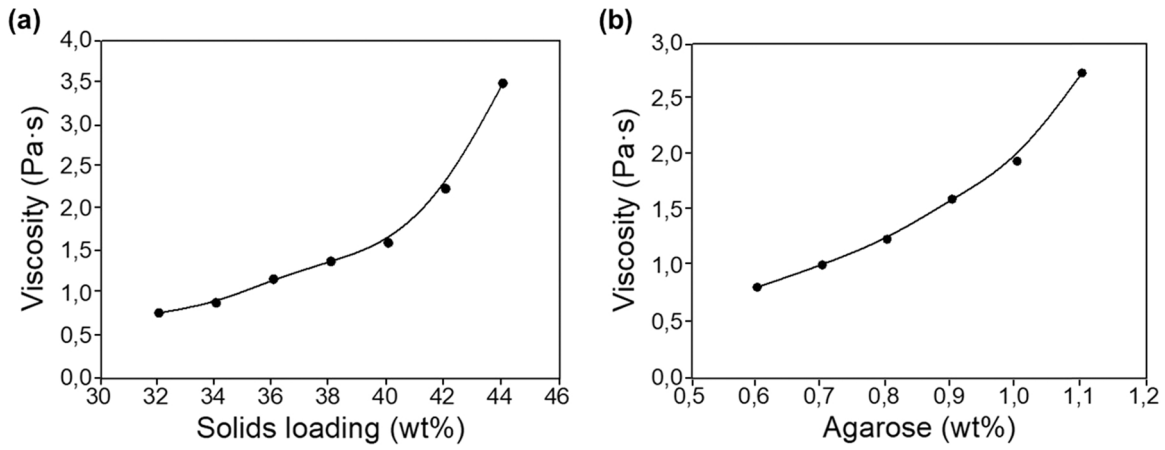

Fig. 4. Viscosity of aqueous solution as a function of: (a) solids loading (vs water) for 0.9 wt% agarose, and (b) agarose (vs water) for 40 wt% solids loading at 60 ºC and a constant shear rate of 100 s^{-1}.

reaches high values of viscosity, which are not suitable for casting planar green bodies using our home-made gel-casting system. Therefore, 40 wt % was selected as the most suitable solids loading to obtain a good viscosity for casting, and a relative high solids loading to minimize the support shrinkage during drying and sintering processes. In order to increase the porosity of the supports, 10 and 15 wt% rice starch (vs. solids loading), as a pore former, were added in the suspensions 1 and 2, respectively. In these formulations, the solids loading content of the suspensions was decreased to 38 and 36 wt%, respectively. These solids loading amounts are slightly lower than that of support 0, without adding pore former, to keep a suitable viscosity of the suspension for casting. Finally, the agarose solution was added to the NiO-GDC suspensions, which increased significantly the viscosity of the suspension, even adding small contents of agarose (Fig. 4b). Since the viscosity increases linearly with the agarose content from 0.6 wt% to 0.9 wt%, and a strong augment in viscosity is reached at 1.0 wt%, the most suitable agarose amount is 0.9 wt% in order to obtain casted green bodies with enough mechanical strength during drying process.

3.3. Microstructural and mechanical characterization of supports

Fig. 5a shows the SEM images of Ni-GDC supports-0, − 1, and − 2, with 0, 10 and 15 wt% rice starch, respectively, after reduction process of NiO-GDC supports in pure H_2 at 750 ºC. Pores (black contrast) can be observed in two different morphologies. Ones with sizes of micrometer range (macroporous, 2–4 μm) and spherical like form mainly generated by the pore former, whereas the others (sub-microporous, 200–500 nm) are conforming an interconnected pore network created during NiO reduction. The walls of both pore morphologies are homogeneously packed with both Ni (light grey contrast) and GDC (white contrast) phases. The difference in porosity amount and pore size distribution is originated from the amount of pore former added in each formulation of aqueous slurry. The porosity of the Ni-GDC supports-0, − 1, and − 2 is 28 %, 41 % and 47 %, respectively.

Fig. 6 and Table 2 show the results of 4-point bending test and Weibull parameters of the Ni-GDC supports-0, − 1 and − 2. As expected, a significant drop of both the strength and Weibull modulus values with the increase of porosity in the supports is observed. Thus, the supports with increasing porosity may suffer the introduction of larger flaws.

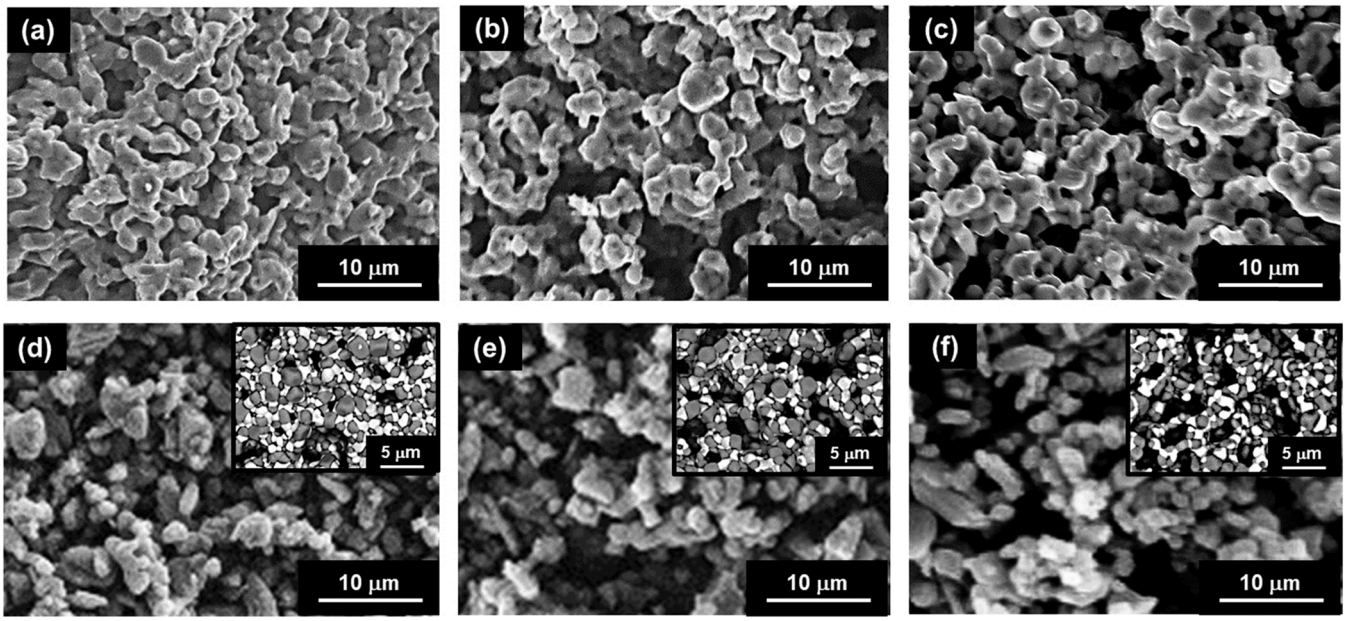

Fig. 5. SEM images in SE mode of: (a) NiO-GDC support-0, (b) − 1, (c) − 2, and (d) Ni-GDC support-0, (e) − 1, and (f) − 2, after sintering and reducing processes, respectively. The inset of images corresponds to the BSE imaging mode.

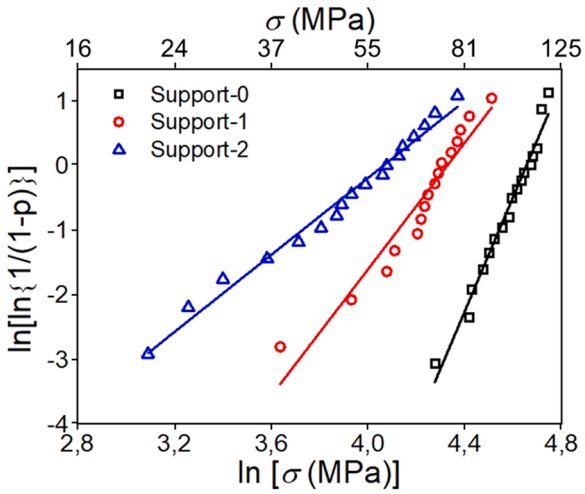

Fig. 6. Weibull plots for the 4-point bending strength tests of the Ni-GDC supports.

Table 2
Bending strength and Weibull parameters of the Ni-GDC supports.

Supports	Strength (MPa)	Weibull parameters	
		Characteristic strength (σ_0, MPa)	Weibull modulus (m)
0	97.0 ± 11.7	105.3	8.9
1	68.2 ± 12.8	75.7	4.9
2	48.9 ± 16.2	58.2	3.0

Support-0 exhibits the best mechanical integrity, but it is not suitable to implement in a SOFC due to its low porosity that limits the gas transport in operation. However, it is interesting to know its mechanical behavior as a reference. Support-1 presents both an average flexural strength value and degree of scatter significantly better than those of support-2, which evidences the negative effect of the extra-porosity on the mechanical strength. Similar trends are also evidenced in Weibull strength and modulus. The strength of SOFC ceramic materials strongly depends on the defects and flaws coming from the manufacturing process, and acting as stress concentrators. According to the obtained results, support-2 may suffer the introduction of larger flaws and defects, and therefore, the failure stress is much more likely to occur. Both the flexural strength value ($\sigma_0 = 75.7$ MPa) and the Weibull modulus (4.9) in support-1 are comparable to those reported in previous works ($\sigma_0 \sim$ 150–60 MPa and m ~ 12–4) for Ni−YSZ planar supports with porosities of 30–45 wt%, which were determined using ring-to-ring, biaxial and 3- or 4-point bending strength tests [29,85–88]. These differences between the present and previous studies may be attributed to the variations in strength of YSZ and GDC, method of mechanical tests, and other material factors such as manufacturing method, composition, porosity, starting materials and microstructure of support. Taking into account this comparative, the mechanical integrity for the support-1 may be the most suitable to fabricate direct-methane SOFCs.

3.4. Optimization of pre-sintering process for supports

Fig. 7 exhibits the shrinkage curve of NiO-GDC support-1 as a function of the sintering temperature. It reveals that the anode supports shrink about 24 % at 1400 °C. This value of support shrinkage is higher than that of GDC pellet (around 17 % at 1400 ºC), which is used as an approximation of electrolyte shrinkage. According to previous studies about the co-sintering of NiO-YSZ/YSZ, NiO-GDC/GDC and NiO-SDC/SDC layered systems [28,29,89,90], several experiments were conducted at pre-sintering temperatures of supports between 900 and

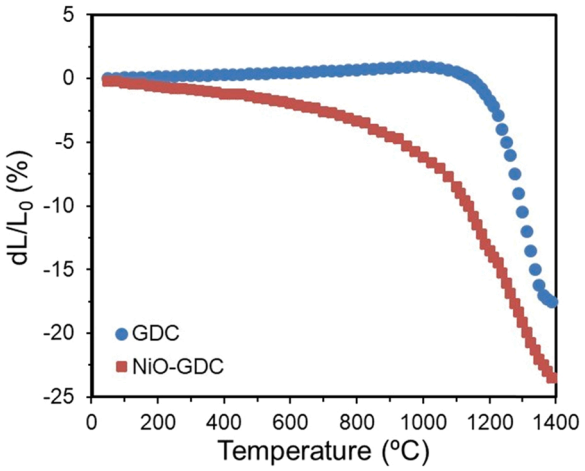

Fig. 7. Linear shrinkage curves during sintering of the NiO-GDC support-1 and GDC pellet in air.

1100 ºC in order to find the optimal cosintering conditions. For pre-sintering temperatures higher than 1000 ºC, the shrinkage of electrolyte is larger than anode support during the co-sintering. Then, both half-cells (support-anode-electrolyte) are concave curved toward the electrolyte layer, due to that the stress of the electrolyte is larger than the strength of the anode support. In addition, some cracks at the electrolyte layer are produced, as the tensile stress is larger than the electrolyte strength. In contrast, the shrinkage of anode support is larger than electrolyte for pre-sintering temperatures lower than 1000 ºC. Then, the half-cell is convex curved and the electrolyte cracked, due to the compressive stress acting on the electrolyte layer. A similar effect was observed in the co-sintering yttria-stabilized zirconia films on anode-supported fuel cell [90]. Thus, a pre-sintering temperature of 1000 ºC for both support-1 and anode is appropriated to obtain a shrinkage of 6 %, as this shrinkage is very close to the difference between the support-1 and electrolyte layer during co-sintering at 1400 ºC.

3.5. Microstructural characterization of cells

Fig. 8 show the microstructures of the cell fabricated with support-1. Fig. 8b exhibits the transverse cross-sectional microstructure of cell at the region of anode/electrolyte/cathode. A good interfacial adhesion between the electrolyte and both electrodes are also evidenced, which is a crucial aspect for a good cell performance and stability at long-term. Note that the 18 ± 1 μm thick GDC electrolyte presents a remarkable density with the typical closed porosity of doped ceria after sintering at 1400 ºC. It guarantees the desired electrolyte gas tightness, which was confirmed during the electrochemical tests, and a relative low ohmic resistance contribution, due to the high ionic conductivity of doped ceria compared to other electrolyte materials like yttria stabilized zirconia [78,91,92]. Finally, both the anode and the cathode present small sizes of particles and pores, thus assuring high active surface areas. Microstructures of Ni–GDC support obtained from SEM, using secondary and backscattered electron detector, are shown in Fig. 8c and d, respectively. In Fig. 8d, black, dark gray and white particles are assigned to pore, Ni and GDC, respectively. Both images evidence that Ni and GDC phases are displayed uniformly distributed, presenting non-agglomerated well-developed grains. It contributes to the lengthened triple phase boundaries (TPBs).

3.6. Electrochemical characterization of cells

Fig. 9a shows the *j*–V and *j*–P curves for the cell fabricated with support-1, operated under humidified H_2 and CH_4/air operation modes, as a fuel, and air, as an oxidant. The electrochemical tests were carried

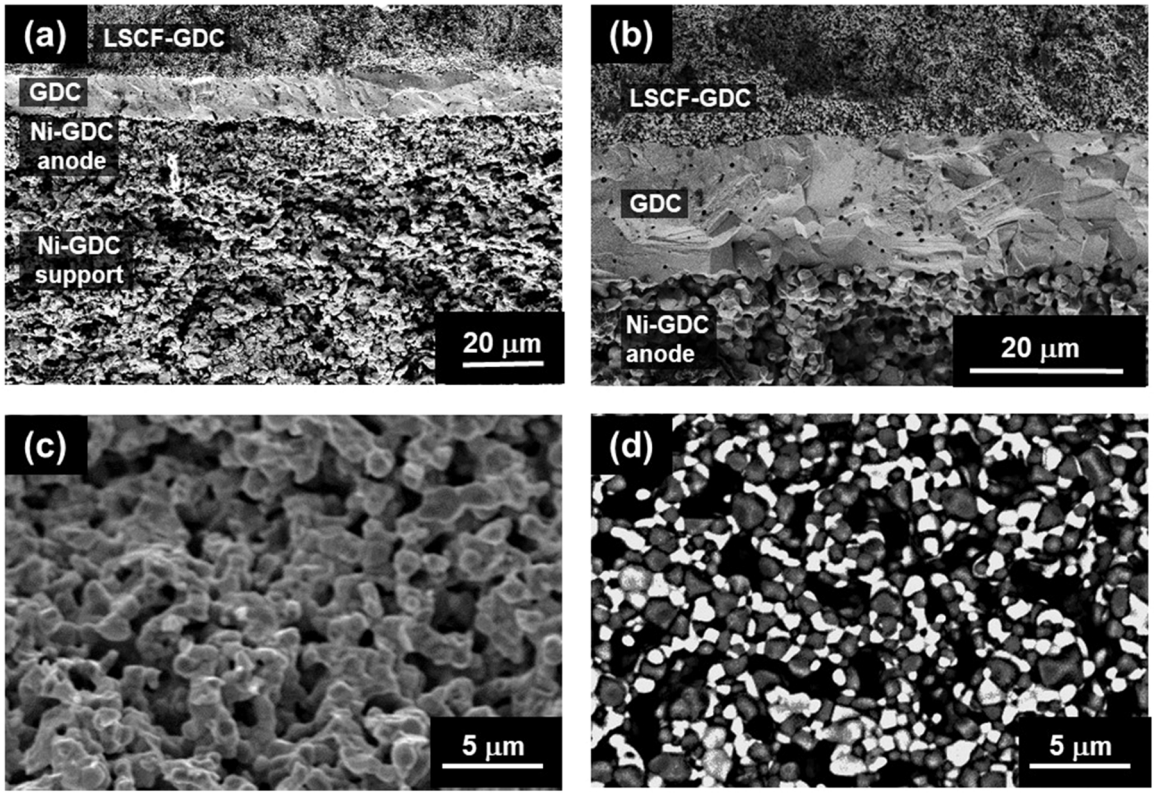

Fig. 8. SEM images of the cell with the Ni-GDC support-1: (a) a general view of the cross section, and (b) the cathode/electrolyte/anode region in SE imaging mode. SEM images of Ni-GDC support obtained in: (c) SE imaging mode, and (d) BSE imaging mode (black, dark grey and white zones are ascribable to pore, Ni and GDC, respectively).

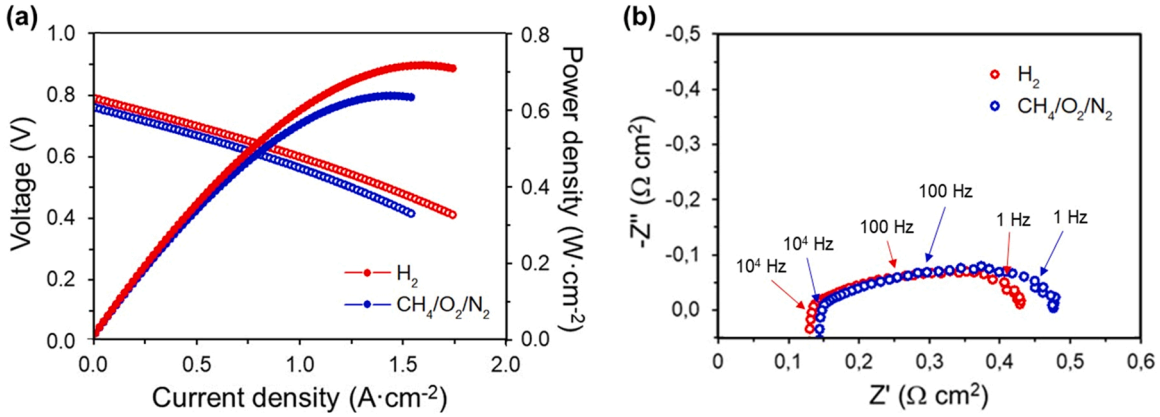

Fig. 9. **(a)** *j*-V and *j*-P curves for Cell-1, and **(b)** Nyquist plots of the EIS spectra measured at 650 ºC under OCV conditions, using 80 ml·min^{-1}·cm^{-2} humidified H_2 (280 ml·min^{-1}·cm^{-2} mixture of $CH_4/O_2/N_2$ = 2/1/4 v/v) at the anode and 200 ml·min^{-1}·cm^{-2} synthetic air at the cathode.

out at 80 ml·min^{-1}·cm^{-2} humidified H_2 and 280 ml·min^{-1}·cm^{-2} mixture of $CH_4/O_2/N_2$ = 2/1/4 v/v at the anode, respectively, and 200 ml·min^{-1}·cm^{-2} synthetic air at the cathode. Maximum power densities of 0.71 and 0.64 W·cm^{-2} were obtained for humidified H_2 and CH_4/air, respectively, operating at 650 ºC. Changing the fuel from H_2 to CH_4/Air, the OCV value drops from 0.80 to 0.76 V. The variation of both OCV and power density is attributed to the changes of fuel gas compositions in different operation modes, due to the reduction of concentration in active fuel (H_2 and CO) in the anode chamber compared to the humidified H_2 operation mode. Although the total fuel flow for the CH_4/Air operation mode is higher than the humidified H_2 operation, due to that 1 mol CH_4 could be potentially reformed to 1 mol CO + 2 mol H_2 compared to the 1 mol H_2 supplied in humidified H_2, the dilution of fuel for the CPOX present more impact on the performance than the fuel transport to the active sites. This interpretation is in concordance with EIS results (Fig. 9b), as higher polarization resistances were reached under CH_4/Air operation. In any case, the arc shapes and peak frequencies in both operation modes are very similar. It suggests that the fuel gases in the electrochemically active anode region under CH_4/Air operation may be quite similar to those of humidified H_2. Therefore, the internal catalytic reforming and the electrochemical oxidation of CH_4, which is much more difficult than that of H_2 or CO, does not takes place in the vicinity of the anode active region. It means that the anode support presents a good performance for the partial oxidation of CH_4 and the anode for the electrochemical oxidation of H_2 and CO. This finding is attributed to a homogeneous distribution of both Ni and GDC phases,

and also an equilibrated combination of macro and micro-porosity, which certainly benefits the gas transport and also the presence of active sites for gas adsorption/desorption processes and catalytic reaction.

Performance stability tests of cell with support-1 were performed in OCV and galvanostatic SOFC mode at a fixed current density of 0.3 A·cm^{-2}, at 650 ºC, using CH_4 as fuel with CH_4/O_2 ratio of 2.0. As shown in Fig. 10a, no degradation on the OCV value was observed after 80 h, evidencing the good stability of Ni-GDC anode and support under CH_4/air as fuel. The good performance and stability for promoting the internal catalytic reforming of methane towards catalytic partial oxidation was exhibited in Fig. 10b, producing H_2 and CO for the anode electrochemical oxidation reactions. Subsequent to this experiment, the cell was switched to SOFC mode by fixing the current density at 0.3 A·cm^{-2} (Fig. 11a). In the first 10 h of the test, the cell displayed around 0.7 V, in agreement with Fig. 10a. However, the performance gradually drops around 0.55 V after 60 h under operation. In Fig. 11b, EIS tests confirmed an increase on the ohmic resistance around 0.09 Ω·cm^{-2} and the polarization resistance around 0.09 Ω·cm^{-2} for the cell operating at 0.3 A·cm^{-2}. This ohmic resistance increase could be due to re-oxidation of Ni and/or delamination at the current-collectors/electrode/electrolyte interfaces. These hypotheses will be later confirmed by SEM post-test analysis.

Owing to the hypothetical importance of feed composition on the degradation of performance, additional stability tests are investigated in CH_4/air operation mode, at the CH_4/O_2 ratios of 2.5 and 3.0, in galvanostatic SOFC mode at a fixed current density of 0.3 A·cm^{-2} (Fig. 11c-e). At the CH_4/O_2 ratio of 2.5, the performance stability of the cell was improved with a slower degradation rate compared to the CH_4/O_2 ratio of 2.0 (Fig. 11c). In Fig. 11d, EIS test also corroborates an increase of the ohmic resistance (around 0.03 Ω·cm^{-2}) and polarization resistance (around 0.05 Ω·cm^{-2}) lower than operating at CH_4/O_2 ratio of 2.0. In contrast, the cell presents a strong performance degradation at a CH_4/O_2 ratio of 3.0 (Fig. 11c). During the first operation hours, the voltage was slightly increased, but in the next 30 h, it progressively decreases to the cell cracked. This behavior is typically attributed to the effect of carbon deposition at the anode and support. Carbon deposits initially cause an increase in the conductivity of anode and support, favoring an improvement of cell performance. After that, the accumulation of the carbon deposits covers the active sites and clogs the pores, resulting in a strong degradation of cell performance. The post-test analysis will also confirm the main degradation mechanisms at different CH_4/O_2 ratios.

3.7. Post-test analysis

Fig. 12 shows post-mortem SEM micrographs of the fracture cross-section at the cathode/electrolyte/anode region, after stability tests. As it can be observed, no cracking or delamination at the interfaces was detected. The dense GDC electrolyte layer is well adhered to the anode and cathode. Fig. 13 exhibits the as-prepared and post-mortem SEM micrographs of the polished cross-section at the cathode and anode regions. The comparison of samples after reduction process and stability tests evidences no remarkable microstructural change in the electrodes.

On the other hand, SEM-EDX analysis at the Ni-GDC support detected the formation of carbon in the cell operated at a CH_4/O_2 ratio of 3.0 (Fig. 14). It confirms the main cause of the strong degradation on the electrochemical performance observed at the highest CH_4/O_2 ratio. In contrast, the presence of carbon is not detected from SEM-EDX in the cells operated at higher oxygen partial pressures (CH_4/O_2 ratio of 2.5). It suggests that Ni reoxidation can take place operating at these CH_4/O_2 ratios. XPS analysis was performed to determine the oxidation states of Ni after operation. Fig. 15 shows the Ni $2p_{3/2}$ XPS spectra for the analysis of Ni-GDC support at the free surface of the support (the fuel entry side) for the cells, after stability tests, operating at the CH_4/O_2 ratios of 2.0 and 2.5. The peaks observed in Ni $2p_{3/2}$ spectra at binding energies of 852.6, 854.6, and 856.1 eV can be assigned to Ni^0, Ni^{2+}, and Ni^{3+}, respectively [93]. For the cell operated at a CH_4/O_2 ratio of 2.0, the deconvolutions of Ni^0, Ni^{2+} and Ni^{3+} peaks determine values of 45 %, 31 %, and 24 %, respectively (Fig. 15a). In contrast, Ni^0 and Ni^{2+} peaks are only observed in the support of the cell operated at a CH_4/O_2 ratio of 2.5, obtaining fractions of 72 %, and 28 % respectively (Fig. 15b). These observations suggest that Ni is mainly present in its metallic state at the free surface of Ni-GDC support, which is the cell region with more exposition to oxygen, but it is partially oxidized depending on CH_4/O_2 ratio. Therefore, higher degradation rate of cell performance at a CH_4/O_2 ratio of 2.0 compared to that of 2.5 can be attributed to the large fraction of Ni re-oxidation during operation.

4. Conclusions

Direct-methane SOFCs operated under mixtures of CH_4 and air have been successfully carried out using a Ni-GDC anode-supported cell. A simple and scalable method based on aqueous gel-casting technique has been developed to fabricate planar supports, starting from nano-composite NiO-GDC powders. Three aqueous slurries formulations of NiO–GDC for gel-casting have been prepared varying the porosity supports, using 0, 10 and 15 wt% rice starch, as a pore former. The mechanical integrity of the Ni-GDC support with 10 wt% rice starch was

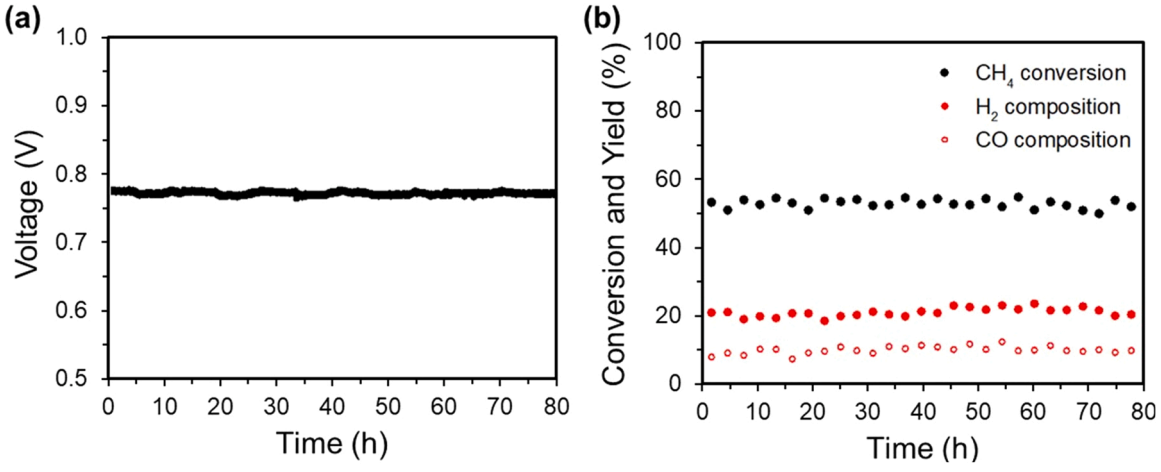

Fig. 10. Evolution of: (a) the voltage, (b) CH_4 conversion, and H_2 and CO yields, for a cell with support-1 in OCV conditions at 650 ºC, under 280 ml·min^{-1}·cm^{-2} methane and air mixture ($CH_4/O_2/N_2$ = 2:1:4 v/v) at the anode and 200 ml·min^{-1}·cm^{-2} synthetic air at the cathode.

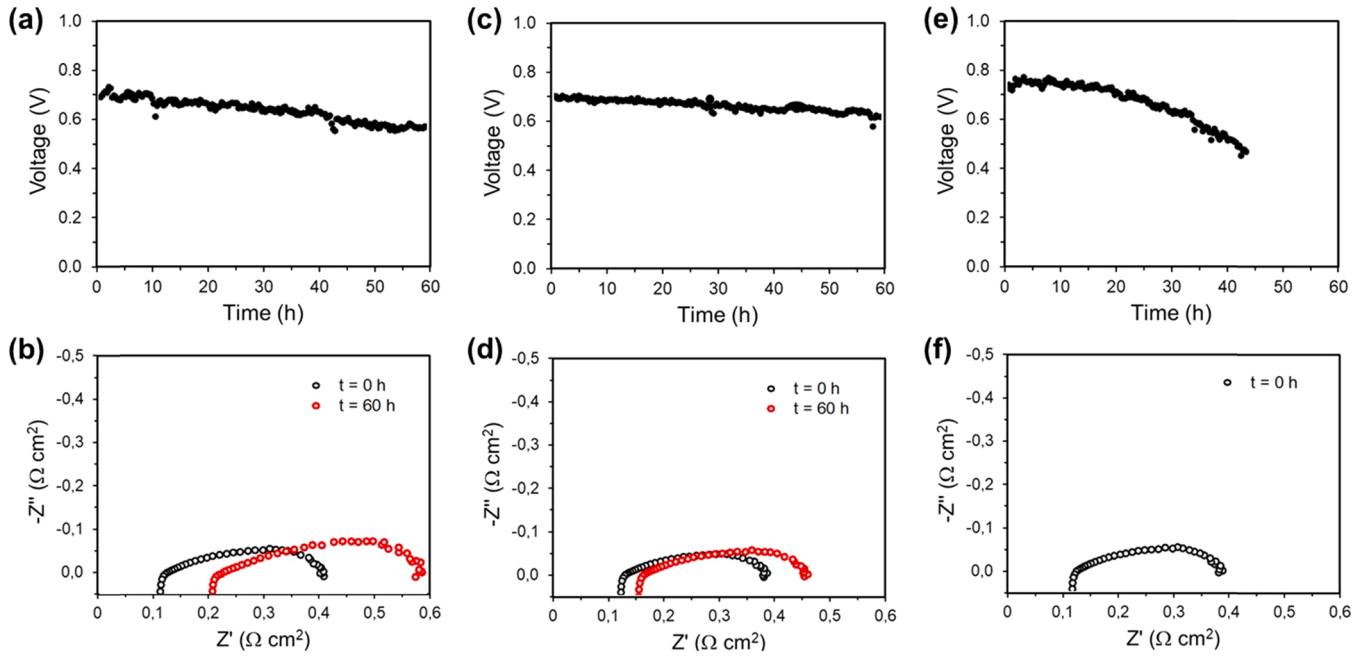

Fig. 11. Evolution of the voltage, and the corresponding Nyquist plots of the EIS spectra, operating at 650 ºC and a fixed current density at 0.3 A·cm^{-2}, under CH_4/air mixtures with a CH_4/O_2 ratio of: (a-b) 2.0, (c-d) 2.5, and (e-f) 3.0. EIS spectrum under a CH_4/air ratio of 3.0 after 40 h is not presented, due to the electrochemical oscillations of cell.

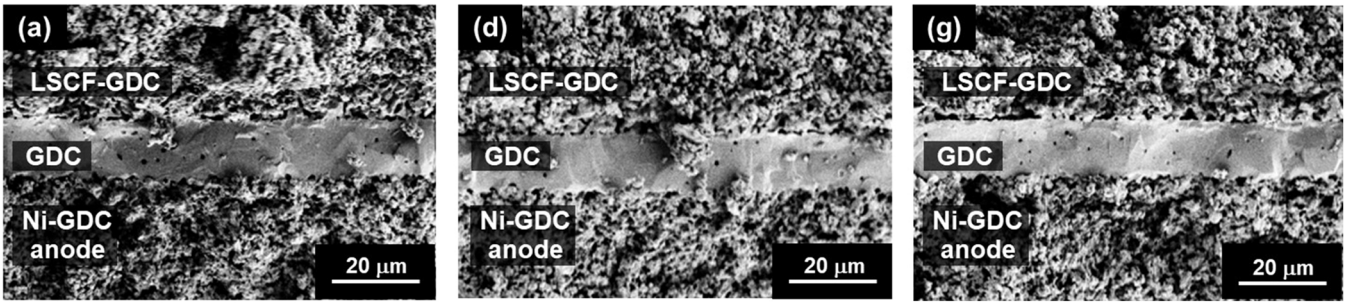

Fig. 12. SEM images in SE mode of the fracture cross-section areas of the cells at the cathode/electrolyte/anode region, after operation at a CH_4/O_2 ratio of: (a) 2.0, (b) 2.5, and (c) 3.0.

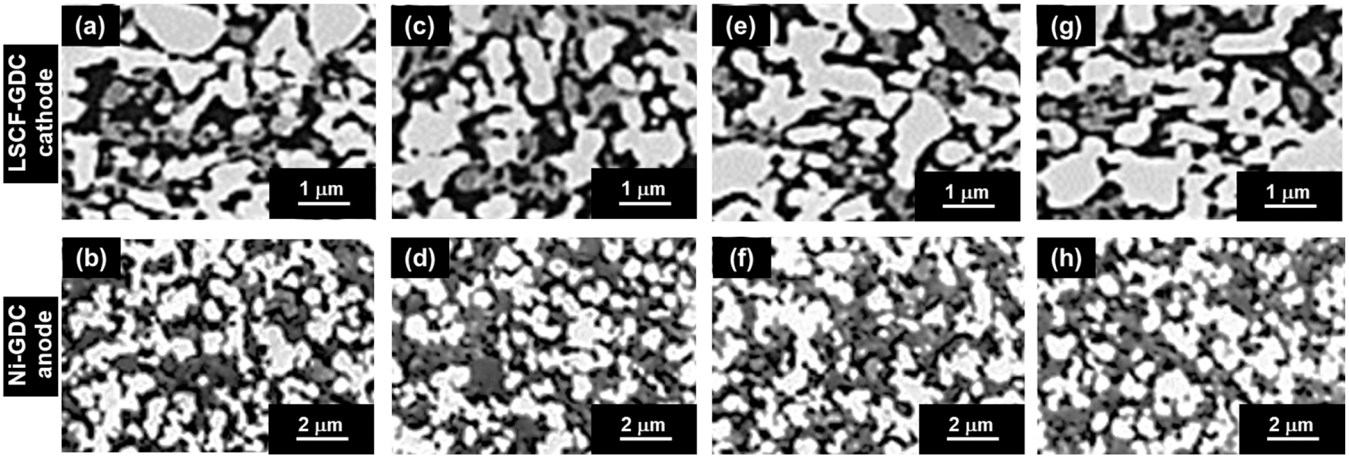

Fig. 13. SEM images in IL-SE mode of the polished cross-section area at the cathode and anode: (a-b) as-prepared and reduced, and after operation at a CH_4/O_2 ratio of: (c-d) 2.0, (e-f) 2.5, and (g-h) 3.0. Note that black, dark grey and white zones are ascribable to pore, GDC and LSCF or Ni, respectively.

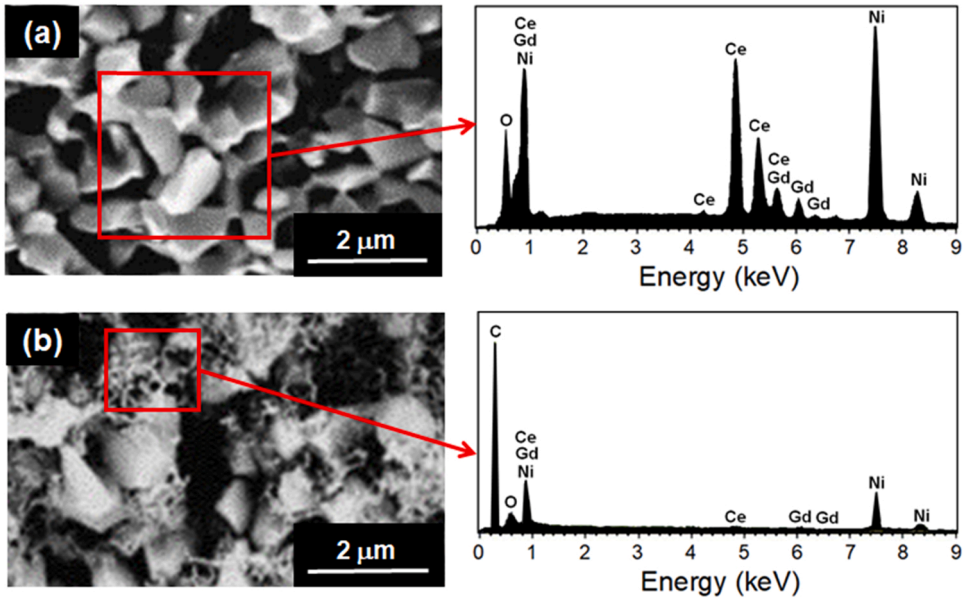

Fig. 14. SEM image in SE mode and EDX spectra determined at the support, after operation, at a CH_4/O_2 ratio of: **(a)** 2.5, **(b)** 3.0, under SOFC mode.

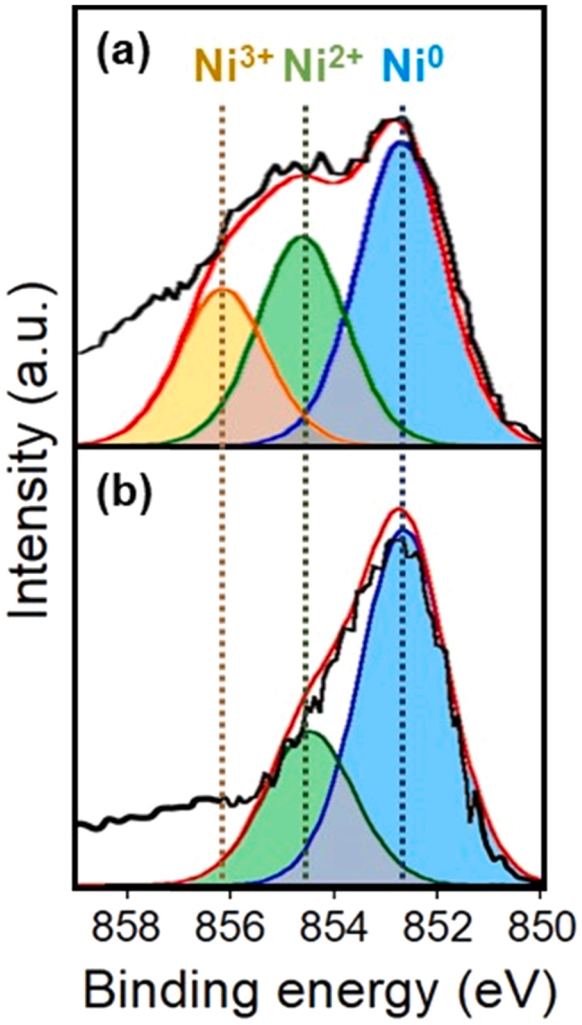

Fig. 15. XPS spectra determined at the free surface of support, after operation 60 h, at a CH_4/O_2 ratio of: **(a)** 2.0 and **(b)** 2.5, under SOFC mode.

found to be suitable for SOFC cell production. Despite the moderated porosity and relative good bending strength of this support, remarkable cell performances are reached at 650 °C for humidified H_2 (0.71 $W{\cdot}cm^{-2}$) and CH_4/air (0.64 $W{\cdot}cm^{-2}$). No significant degradation of OCV is observed under CH_4/air after 80 h. In addition, a stable CH_4 conversion and production of H_2 and CO are achieved under OCV conditions. It suggests that the Ni-GDC anode support presents a good performance and stability for promoting the internal catalytic reforming of methane towards CPOX. In contrast, the performance gradually drops in galvanostatic SOFC mode at a fixed current density of 0.3 $A{\cdot}cm^{-2}$. The degradation rate strongly depends on CH_4/O_2 ratio, as it is associated to that Ni anode suffer from occasional oxidation at the lowest CH_4/O_2 ratio of 2.0, increasing ohmic resistance, to carbon deposition at the highest CH_4/O_2 ratio of 3.0, thus deteriorating the electrochemical performance. The best electrochemical stability of the cell is achieved at a CH_4/O_2 ratio of 2.5, showing no evidence of carbon deposition and reducing nickel re-oxidation significantly.

This study reveals that NiO–GDC nanocomposite supports fabricated by gel-casting are a promising solution for direct-methane SOFCs operated under mixtures of CH_4 and air. It prevents the deactivation of Ni catalysts, ensuring a good activity of the CPOX reaction, and avoiding an important oxidation and carbon coking-induced poisoning of Ni. However, more improvements are still required, such as a better optimization of air addition to fuel and total methane-air flow, which are crucial issues to guarantee stable performance under operation conditions. The effect of CH_4/air ratio and the total methane-air flow on the electrochemical performance of SOFCs should be further investigated including long-term studies.

Declaration of Competing Interest

The authors declare that they have no known competing financial interests or personal relationships that could have appeared to influence the work reported in this paper.

Acknowledgements

This research has received funding from grants PGC2018-096855-B-C41 and PID2019-107106RB-C32 funded by MCIN/AEI/10.13039/501100011033. Miguel Morales Comas is a Serra Húnter Fellow (Generalitat de Catalunya).

References

[1] EG&G Technical Services, Inc. Fuel Cell Handbook (Seventh Edition). University Press of the Pacific, 2004.

[2] J. Larmine, A.Dicks Fuel, Cell Systems Explained, John Wiley & Sons, Chichester, UK, 2006.

[3] F.-Y. Liang, M. Ryvak, S. Sayeed, N. Zhao, The role of natural gas as a primary fuel in the near future, including comparisons of acquisition, transmission and waste handling costs of as with competitive alternatives, Chem. Cent. J. 6 (S4) (2012) 1–24, https://doi.org/10.1186/1752-153X-6-S1-S4.

[4] M. Qadrdan, M. Abeysekera, M. Chaudry, J. Wu, N. Jenkins. Role of power-to-gas in an integrated gas and electricity system in Great Britain, Int. J. Hydrog. Energy 40 (17) (2015) 5763–5775, https://doi.org/10.1016/j.ijhydene.2015.03.004.

[5] Zengjia Guo Qidong Xu, Qijiao He Lingchao Xia, Idris Temitope Bello Zheng Li, Meng Ni Keqing Zheng, A comprehensive review of solid oxide fuel cells operating on various promising alternative fuels, Energy Conv. Manag. 253 (2022), 115175, https://doi.org/10.1016/j.enconman.2021.115175.

[6] M. Götz, J. Lefebvre, F. Mörs, A. McDaniel Koch, F. Graf, S. Bajohr, R. Reimert, T. Kolb, Renewable Power-to-Gas: a technological and economic review, Renew. Energy 85 (2016) 1371–1390, https://doi.org/10.1016/j.renene.2015.07.066.

[7] J. Macek, B. Novosel, M. Marinsek, Ni-YSZ SOFC anodes - minimization of carbon deposition, J. Eur. Ceram. Soc. 27 (2007) 487–491, https://doi.org/10.1016/j.jeurceramsoc.2006.04.107.

[8] A.J. Jacobson, Materials for solid oxide fuel cells, Chem. Mater. 22 (2010) 660–674, https://doi.org/10.1021/cm902640j.

[9] P. Boldrin, E. Ruiz-Trejo, J. Mermelstein, J.M. Bermudez Menendez, T. Ramirez Reina, N.P. Brandon, Strategies for carbon and sulfur tolerant solid oxide fuel cell materials, incorporating lessons from heterogeneous catalysis, Chem. Rev. 116 (2016) 13633–13684, https://doi.org/10.1021/acs.chemrev.6b00284.

[10] B.C. Steele, Fuel-cell technology: Running on natural gas, Nature 400 (1999) 619, https://doi.org/10.1038/23144.

[11] Y. Ling, X. Wang, Z. Ma, K. Wei, Y. Wu, M. Khan, K. Zheng, S. Shen, S. Wang, Review of experimental and modelling developments for ceria-based solid oxide fuel cells free from internal short circuits, J. Mater. Sci. 55 (2020) 1–23, https://doi.org/10.1007/s10853-019-03876-z.

[12] Z. Lyu, Y. Wang, Y. Zhang, M. Han, Solid oxide fuel cells fueled by simulated biogas: comparison of anode modification by infiltration and reforming catalytic layer, Chem. Eng. J. 393 (2020), 124755, https://doi.org/10.1016/j.cej.2020.124755.

[13] H. Su, Y.H. Hu, Progress in low-temperature solid oxide fuel cells with hydrocarbon fuels, Chem. Eng. J. 402 (15) (2020), 126235, https://doi.org/10.1016/j.cej.2020.126235.

[14] J.-H. Myung, H.-J. Ko, J.-J. Lee, J.-H. Lee, S.-H. Hyun, Synthesis and characterization of NiO/GDC–GDC dual nano-composite powders for high-performance methane fueled solid oxide fuel cells, Int. J. Hydrog. Energy 37 (2012) 11351–11359, https://doi.org/10.1016/j.ijhydene.2012.04.140.

[15] C.D. Ding, K. Sato, J. Mizusaki, T. Hashida, A comparative study of $NiO–Ce_{0.9}Gd_{0.1}O_{1.95}$ nanocomposite powders synthesized by hydroxide and oxalate co-precipitation methods, Ceram. Int. 38 (2012) 85–92, https://doi.org/10.1016/j.ceramint.2011.06.041.

[16] J.R. Wilson, W. Kobsiriphat, R. Mendoza, H.Y. Chen, J.M. Hiller, D.J. Miller, et al., Three-dimensional reconstruction of a solid-oxide fuel-cell anode, Nat. Mater. 5 (2006) 541–544, https://doi.org/10.1038/nmat1668.

[17] S. Suda, S. Takahashi, M. Kawano, H. Yoshida, T. Inagaki, Effects of atomization conditions on morphology and SOFC anode performance of spray pyrolyzed $NiO–Sm_{0.2}Ce_{0.8}O_{1.9}$ composite particles, Solid State Ion. 177 (2006) 1219–1225, https://doi.org/10.1016/j.ssi.2006.05.012.

[18] M. Mamak, N. Coombs, G. Ozin, Self-assembling solid oxide fuel cell materials: mesoporous yttria-zirconia and metal-yttria-zirconia solid solutions, J. Am. Chem. Soc. 122 (2000) 8932–8939, https://doi.org/10.1021/ja0013677.

[19] Y. Xie, N. Shi, X. Hu, M. Liu, Y. Yang, D. Huan, Y. Pan, R. Peng, C. Xia, Novel in-situ MgO nano-layer decorated carbon tolerant anode for solid oxide fuel cells, Int. J. Hydrog. Energy 45 (2020) 11791–11801, https://doi.org/10.1016/j.ijhydene.2020.02.117.

[20] B. Tu, Y. Yin, F. Zhang, X. Su, X. Lyu, M. Cheng, High performance of direct methane-fuelled solid oxide fuel cell with samarium modified nickel-based anode, Int. J. Hydrog. Energy 45 (51) (2020) 27587–27596, https://doi.org/10.1016/j.ijhydene.2020.07.070.

[21] P. Li, Z. Wang, X. Yao, Ni Hou, L. Fan, T. Gan, Y. Zhao, Y. Li, J.W. Schwank, Effect of Sn addition on improving the stability of $Ni-Ce_{0.8}Sm_{0.2}O_{1.9}$ anode material for solid oxide fuel cells fed with dry CH_4, Catal. Today 330 (2019) 209–216, https://doi.org/10.1016/j.cattod.2018.04.030.

[22] Y. Lin, Z. Zhan, S.A. Barnett, Improving the stability of direct-methane solid oxide fuel cells using anode barrier layers, J. Power Sources 158 (2006) 1313–1316, https://doi.org/10.1016/j.jpowsour.2005.09.060.

[23] D. Yoon, A. Manthiram, Hydrogen tungsten bronze as a decoking agent for long-life, natural gas-fueled solid oxide fuel cells, Energy Environ. Sci. 7 (2014) 3069–3076, https://doi.org/10.1039/c4ee01455c.

[24] Y. Song, W. Wang, L. Ge, X. Xu, Z. Zhang, P.S.B. Juliao, W. Zhou, Z. Shao, Rational design of a water-storable hierarchical architecture decorated with amorphous barium oxide and nickel nanoparticles as a solid oxide fuel cell anode with excellent sulfur tolerance, Adv. Sci. 4 (2017) 1700337, https://doi.org/10.1002/advs.201700337.

[25] L. Almar, B. Colldeforns, L. Yedra, S. Estrade, F. Peiró, A. Morata, A. Tarancón, High temperature long-term stable ordered mesoporous Ni–CGO as an anode for solid oxide fuel cells, J. Mater. Chem. A 1 (2013) 4531–4538, https://doi.org/10.1039/c3ta10439g.

[26] D. Tian, W. Liu, Y. Chen, W. Yu, L. Yu, B. Lin, A robust $NiO–Sm_{0.2}Ce_{0.8}O_{1.9}$ anode for direct-methane solid oxide fuel cell, Mater. Res. Bull. 71 (2015) 1–6, https://doi.org/10.1016/j.materresbull.2015.06.042.

[27] Z. Wang, S. Wang, S. Jiao, W. Weng, K. Cheng, B. Qian, H. Yu, Y. Chao, A hierarchical porous microstructure for improving long-term stability of $Ni_{1-x}Cu_x$/SDC anode-supported IT-SOFCs fueled with dry methane, J. Alloy. Compd. 702 (2017) 186–192, https://doi.org/10.1016/j.jallcom.2017.01.212.

[28] Z. Wang, J. Qian, J. Cao, S. Wang, T. Wen, A study of multilayer tape casting method for anode-supported planar type solid oxide fuel cells (SOFCs), J. Alloy. Compd. 437 (1–2) (2007) 264–268, https://doi.org/10.1016/j.jallcom.2006.07.110.

[29] N.H. Menzler, J. Malzbender, P. Schoderböck, R. Kauert, H.P. Buchkremer, Sequential Tape Casting of Anode Supported Solid Oxide, Fuel Cells Fuel Cells 14 (1) (2014) 96–106, https://doi.org/10.1002/fuce.201300153.

[30] L. Bernadet, M. Morales, X.G. Capdevila, F. Ramos, M.C. Monterde, J.A. Calero, A. Morata, M. Torrell, A. Tarancón, Reversible fuel electrode supported solid oxide cells fabricated by aqueous multilayered tape casting, J. Phys. Energy 3 (2021), 024002, https://doi.org/10.1088/2515-7655/abd296.

[31] X. Wang, L. Jia, K. Li, D. Yan, B. Chi, J. Pu, L. Jian, Porous nickel-iron alloys as anode support for intermediate temperature solid oxide fuel cells: II. Cell performance and stability, Int. J. Hydrog. Energy 43 (2018) 21030–21036, https://doi.org/10.1016/j.ijhydene.2018.09.142.

[32] J. Kupecki, R. Kluczowski, D. Papurello, A. Lanzini, M. Kawalec, M. Krauz, M. Santarelli, Characterization of a circular 80 mm anode supported solid oxide fuel cell (AS-SOFC) with anode support produced using high-pressure injection molding (HPIM), Int. J. Hydrog. Energy 44 (2019) 19405–19411, https://doi.org/10.1016/j.ijhydene.2018.02.143.

[33] Y. Zhang, J. Gao, G. Meng, X. Liu, Production of dense yttria-stabilized zirconia thin films by dip coating for IT-SOFC application, J. Appl. Electrochem. 34 (2004) 637–641, https://doi.org/10.1023/B:JACH.0000021926.97895.f7.

[34] X. Shao, W.D.A. Rickard, D. Dong, H. Dang, M. Saunders, A. Dodd, G. Parkinson, C.-Z. Li, High performance anode with dendritic porous structure for low temperature solid oxide fuel cells, Int. J. Hydrog. Energy 43 (2018) 17849–17856, https://doi.org/10.1016/j.ijhydene.2018.07.171.

[35] L. Montanaro, B. Coppola, P. Palmero, J.-M. Tulliani, A review on aqueous gelcasting: A versatile and low-toxic technique to shape ceramics, Ceram. Int. 45 (2019) 9653–9673, https://doi.org/10.1016/j.ceramint.2018.12.079.

[36] I. Santacruz, M.A. Nieto, R. Moreno, Alumina bodies with near-to-theoretical density by aqueous gel casting using concentrated agarose solutions, Ceram. Int. 31 (2005) 439–445, https://doi.org/10.1016/j.ceramint.2004.06.007.

[37] W.H. Kok, W.K.C. Yung, D.T.C. Ang, Green gelcasting of aluminum nitride using environmental sustainable ovalbumin natural binder, J. Aust. Ceram. Soc. (2018) 1–9, https://doi.org/10.1007/s41779-018-0222-3.

[38] X. He, B. Su, X. Zhou, J. Yang, B. Zhao, X. Wang, G. Yang, Z. Tang, H. Qiu, Gelcasting of alumina ceramics using egg white protein binder system, Ceram. Silik. 55 (2011) 1–7.

[39] A.J. Millán, M.I. Nieto, R. Moreno, Near-net shaping of aqueous alumina slurries using carrageenan, J. Eur. Ceram. Soc. 22 (2002) 297–3030, https://doi.org/10.1016/S0955-2219(01)00283-7.

[40] J. Xu, Y. Zhang, K. Gan, X. Zhang, Y. Qu, N. Ma, J. Yang, A novel gelcasting of alumina suspension using curdlan gelation, Ceram. Int. 41 (2015) 10520–10525, https://doi.org/10.1016/j.ceramint.2015.04.144.

[41] Y. Chen, Z. Xie, J. Yang, Y. Huang, Alumina casting based on gelation of gelatine, J. Eur. Ceram. Soc. 19 (1999) 271–275, https://doi.org/10.1016/S0955-2219(98)00201-5.

[42] Y. Jia, Y. Kanno, Z.P. Xie, New gelcasting process for alumina ceramics based on gelation of alginate, J. Eur. Ceram. Soc. 22 (2002) 1911–1916, https://doi.org/10.1016/S0955-2219(01)00513-1.

[43] L. Chen, X.L. Song, J.D. Ye, B. Li, Colloidal in-situ consolidation forming of Al_2O_3 ceramics using modified starch, Key Eng. Mater. 280 (2005) 1027–1032, https://doi.org/10.4028/www.scientific.net/kem.280-283.1027.

[44] L. Yuan, Z. Liu, X. Hou, C. Tian, Q. Zhu, S. Wang, B. Ma, J. Yu, A novel aqueous gel-casting for fabricating Al_2O_3-bonded fibrous mullite ceramics, J. Alloy. Compd. 811 (2019), 152009, https://doi.org/10.1016/j.jallcom.2019.152009.

[45] S.K. Swain, D.K. Sengupta, B.P. Singh, S. Bhattacharjee, Gelcasting-a versatile process, Part 1. Int. Ceram. 54 (2005) 174–177.

[46] R. Gilissen, J.P. Erauw, A. Smolders, E. Vanswijgenhoven, J. Luyten, Gelcasting, a Net. shape Tech., Mater. Des. 21 (2000) 251–257, https://doi.org/10.1016/S0261-3069(99)00075-8.

[47] A. Rincón, G. Giacomello, M. Pasetto, E. Bernardo, Novel 'inorganic gel casting' process for the manufacturing of glass foams, J. Eur. Ceram. Soc. 37 (5) (2017) 2227–2234, https://doi.org/10.1016/j.jeurceramsoc.2017.01.012.

[48] J.J. Nick, D. Newson, B. Draskovich, O.O. Omatete Gelcasting advancement for manufacturing scale-up, in: Proceedings of the 23rd Annual Cocoa Beach International Conference on Engineering Ceramics and Structures. Cocoa Beach, Florida, January 24–29, 1999.

[49] J.J. Nick, D. Newson, R. Masseth, S. Monette Gelcasting automation for high volume production of silicon nitride turbine weels, in: Proceedings of the 23rd Annual Cocoa Beach International Conference on Engineering Ceramics and Structures. Cocoa Beach, Florida, January 24–29, 1999, pp. 225–232. https://doi.org/10.1007/S41779–018-0222–3.

[50] B. Su, S. Dhara, L. Wang, Green ceramic machining: a top-down approach for the rapid fabrication of complex-shaped ceramic, J. Eur. Ceram. Soc. 28 (2008) 2109–2115, https://doi.org/10.1016/j.jeurceramsoc.2008.02.023.

[51] M.E. Navarro, X.G. Capdevila, M. Morales, J.J. Roa, M. Segarra, Manufacturing of anode-supported tubular solid oxide fuel cells by a new shaping technique using aqueous gel-casting, J. Power Sources 200 (2012) 45–52, https://doi.org/10.1016/j.jpowsour.2011.10.059.
[52] O.O. Omatete, M.A. Janney, S.D. Nunn, Gelcasting: from laboratory development to industrial production, J. Eur. Ceram. Soc. 17 (1997) 407–413, https://doi.org/10.1016/S0955-2219(96)00147-1.
[53] M. Morales, M.E. Navarro, X.G. Capdevila, J.J. Roa, M. Segarra, Processing of graded anode-supported micro-tubular sofcs based on samaria-doped ceria via gel-casting and spray-coating, Ceram. Int. 38 (2012) 3713–3722, https://doi.org/10.1016/j.ceramint.2012.01.015.
[54] M. Morales, M.A. Laguna-Bercero, M.E. Navarro, F. Espiell, M. Segarra, The effect of anode support on the electrochemical performance of microtubular solid oxide fuel cells fabricated by gel-casting, RSC Adv. 5 (2015) 39350–39357, https://doi.org/10.1039/C5ra02304a.
[55] M. Morales, M.A. Laguna-Bercero, Microtubular solid oxide fuel cells fabricated by gel-casting: the role of supporting microstructure on the mechanical properties, RSC Adv. 7 (2017) 17620–17628, https://doi.org/10.1039/c7ra01259d.
[56] M. Morales, M.A. Laguna-Bercero, Influence of anode functional layers on electrochemical performance and mechanical strength in microtubular solid oxide fuel cells fabricated by gel-casting, ACS Appl. Energy Mater. 1 (5) (2018) 2024–2031, https://doi.org/10.1021/acsaem.8b00115.
[57] S. McIntosh, R.J. Gorte, Direct hydrocarbon solid oxide fuel cells, Chem. Rev. 104 (2004) 4845–4866, https://doi.org/10.1021/cr020725g.
[58] Z. Lyu, H. Li, M. Han, Electrochemical properties and thermal neutral state of solid oxide fuel cells with direct internal reforming of methane, Int. J. Hydrog. Energy 44 (23) (2019) 12151–12162, https://doi.org/10.1016/j.ijhydene.2019.03.048.
[59] J.A. Liu, S.A. Barnett, Operation of anode-supported solid oxide fuel cells on methane and natural gas, Solid State Ion. 158 (2003) 11–16, https://doi.org/10.1016/S0167-2738(02)00769-5.
[60] B. Tu, H. Wen, Y. Yin, F. Zhang, X. Su, D. Cui, M. Cheng, Thermodynamic analysis and experimental study of electrode reactions and open circuit voltages for methane-fuelled SOFC, Int. J. Hydrog. Energy 45 (58) (2020) 34069–34079, https://doi.org/10.1016/j.ijhydene.2020.09.088.
[61] B. Tu, H. Qi, Y. Yin, T. Zhang, D. Liu, S. Han, F. Zhang, X. Su, D. Cui, M. Cheng, Effects of methane processing strategy on fuel composition, electrical and thermal efficiency of solid oxide fuel cell, Int. J. Hydrog. Energy 46 (52) (2021) 26537–26549, https://doi.org/10.1016/j.ijhydene.2021.05.128.
[62] M. Höber, B. Königshofer, G. Pongratz, P. Boškoski, G. Nusev, C. Hochenauer, V. Subotic, Experimental investigation of electrochemical reactions along SOFCs for internal and external reformed methane, ECS Trans. 103 (2021) 2017, https://doi.org/10.1149/10301.2017ecst.
[63] D. Fan, Y. Gao, F. Liu, T. Wei, Z. Ye, Y. Ling, B. Chen, Y. Zhang, M. Ni, D. Dong, Autothermal reforming of methane over an integrated solid oxide fuel cell reactor for power and syngas co-generation, J. Power Sources 513 (2021), 230536, https://doi.org/10.1016/j.jpowsour.2021.230536.
[64] C. Moretti, B. Corona, V. Rühlin, T. Götz, M. Junginger, T. Brunner, I. Obernberger, L. Shen, Combining biomass gasification and solid oxide fuel cell for heat and power generation: an early-stage life cycle assessment, Energies 13 (11) (2020) 2773, https://doi.org/10.3390/en13112773.
[65] N. Laosiripojana, S. Assabumrungrat, Catalytic steam reforming of methane, methanol, and ethanol over Ni/YSZ: the possible use of these fuels in internal reforming SOFC, J. Power Sources 163 (2007) 943–951, https://doi.org/10.1016/j.jpowsour.2006.10.006.
[66] A.L. Dicks, K.D. Pointon, A. Siddle, Intrinsic reaction kinetics of methane steam reforming on a nickel/zirconia anode, J. Power Sources 86 (2000) 523–530, https://doi.org/10.1016/S0378-7753(99)00447-4.
[67] T. Hibino, A. Hashimoto, T. Inoue, J.-I. Tokuno, S.-I. Yoshida, M. Sano, A low operating-temperature solid oxide fuel cell in hydrocarbon-air mixtures, Science 288 (2000) 2031–2033, https://doi.org/10.1126/science.288.5473.2031.
[68] D. Lee, J. Myung, J. Tan, S.-H. Hyun, J.T.S. Irvine, J. Kim, J. Moon, Direct methane solid oxide fuel cells based on catalytic partial oxidation enabling complete coking tolerance of Ni-based anodes, J. Power Sources 345 (2017) 30–40, https://doi.org/10.1016/j.jpowsour.2017.02.003.
[69] Z. Shao, S.M. Haile, J. Ahn, P.D. Ronney, Z. Zhan, S.A. Barnett, A thermally self-sustained solid-oxide fuel-cell stack with high power density, Nature 435 (2005) 795–798, https://doi.org/10.1038/nature03673.
[70] M. Kuhn, T.W.Napporn Single-Chamber Solid Oxide Fuel Cell Technology-From Its, Origins to Today's State of the Art, Energies 3 (1) (2010) 57–134, https://doi.org/10.3390/en3010057.
[71] M. Morales, F. Espiell, M. Segarra, Improvement of performance in low temperature solid oxide fuel cells operated on ethanol and air mixtures using Cu–ZnO–Al_2O_3 catalyst layer, J. Power Sources 293 (2015) 366–372, https://doi.org/10.1016/j.jpowsour.2015.05.097.
[72] M. Morales, J.J. Roa, X.G. Capdevila, M. Segarra, S. Piñol, Anode-supported SOFC operated under single-chamber conditions at intermediate temperatures, Fuel Cells 11 (1) (2011) 108–115, https://doi.org/10.1002/fuce.201000063.
[73] D. Lee, D. Kim, J. Kim, J. Moon, Characterizing nano-scale electrocatalysis during partial oxidation of methane, Sci. Rep. 4 (2014) 3937, https://doi.org/10.1038/srep03937.
[74] H. Aslannejad, L. Barelli, A. Babaie, S. Bozorgmehri, Effect of air addition to methane on performance stability and coking over NiO–YSZ anodes of SOFC, Appl. Energ. 177 (2016) 179–186, https://doi.org/10.1016/j.apenergy.2016.05.127.
[75] M. Farnak, J.A. Esfahani, S. Bozorgmehri, An experimental investigation on flow-rate effects of internal CPOX reforming in SOFCs, Appl. Therm. Eng. 163 (2019), 114411, https://doi.org/10.1016/j.applthermaleng.2019.114411.
[76] Y. Tian, Z. Lü, X. Guo, P. Wu, Catalytic Activity of Ni-YSZ composite as anode for methaneoxidation in solid oxide fuel cells, Int. J. Electrochem. Sci. 14 (2019) 1093–1106, https://doi.org/10.20964/2019.02.48.
[77] Z. Lin, K. Zhao, G. Cheng, S. Hu, M. Chen, J. Li, D. Chen, Q. Xu, M. Chang, O. Volodymyr, Catalyst layer supported solid oxide fuel cells running on methane, J. Power Sources 507 (2021), 230317, https://doi.org/10.1016/j.jpowsour.2021.230317.
[78] M. Morales, J.J. Roa, X.G. Capdevila, M. Segarra, S. Pinol, Effect of sintering temperature on the mechanical properties of film $Gd_{0.2}Ce_{0.8}O_{1.9}$, Electrolyte SOFCs Using Nanoindentation 12 (4) (2009) 171–238, https://doi.org/10.14447/jnmes.v12i4.201.
[79] T.H. Courtney, Mechanical Behavior of Materials, McGraw-Hill,, Singapore, 1990.
[80] A.S.T.M. C1161-02c, Standard Test Method for Flexural Strength of Advanced Ceramics at Ambient Temperature. PA, ASTM International,, West Conshohocken, 2002.
[81] G.D. Quinn, B. Sparenberg, P. Koshy, L.K.S. Jahanmir, D. Arola, Flexural strength of ceramic and glass rods, J. Test. Eval. 37 (3) (2009) 222–244, https://doi.org/10.1520/jte101649.
[82] W. Weibull, A. Statistical Distribution, Function of Wide Applicability, J. Appl. Mech. Trans. (1951) 293–297.
[83] A. Larrea, D. Sola, M.A. Laguna-Bercero, J.I. Peña, R.I. Merino, V.M. Orera, Self-supporting thin yttria-stabilised zirconia electrolytes for solid oxide fuel cells prepared by laser machining, J. Electrochem. Soc. 158 (10) (2011) B1193, https://doi.org/10.1149/1.3619759/xml.
[84] J.A. Cebollero, R. Lahoz, M.A. Laguna-Bercero, J.I. Peña, A. Larrea, V.M. Orera, Characterization of laser-processed thin ceramic membranes for electrolyte-supported solid oxide fuel cells, Int. J. Hydrog. Energ. 42 (19) (2017) 13939–13948, https://doi.org/10.1016/j.ijhydene.2016.12.112.
[85] M. Radovic, E. Lara-Curzio, Mechanical properties of tape cast nickel based anode materials for solid oxide fuel cells before and after reduction in hydrogen, Acta Mater. 52 (2004) 5747–5756, https://doi.org/10.1016/j.actamat.2004.08.023.
[86] E. Lara-Curzio, M. Radovic, M. Trejo, C. Cofer, T. Watkins, K. More, Effect of thermal cycling and thermal aging on the mechanical properties of, and residual stresses in, Ni–YSZ/YSZ bi-layers, Adv. Solid Oxide Fuel Cells II 27 (2007) 383–391, https://doi.org/10.1002/9780470291337.ch37.
[87] A. Nakajo, J. Kuebler, A. Faes, U.F. Vogt, H.J. Schindler, L.-K. Chiang, S. Modena, J.V. Herle, T. Hocker, Compilation of mechanical properties for the structural analysis of solid oxide fuel cell stacks. Constitutive materials of anode-supported cells, Ceram. Int. 38 (5) (2012) 3907–3927, https://doi.org/10.1016/j.ceramint.2012.01.043.
[88] L. Frandsen, T. Ramos, A. Faes, M. Pihlatie, K. Brodersen, Optimization of the strength of SOFC anode supports, J. Eur. Ceram. Soc. 32 (5) (2012) 1041–1052, https://doi.org/10.1016/j.jeurceramsoc.2011.11.015.
[89] M. Chen, B. Hee Kim, Q. Xu, B.G. Ahn, Preparation and electrochemical properties of Ni–SDC thin films for IT-SOFC anode, J. Membr. Sci. 334 (1–2) (2009) 138–147, https://doi.org/10.1016/j.memsci.2009.02.023.
[90] Z. Shen, X. Zhu, S. Le, W. Sun, K. Sun, Co-sintering anode and Y_2O_3 stabilized ZrO_2 thin electrolyte film for solid oxide fuel cell fabricated by co-tape casting, Int. J. Hydrog. Energy 37 (13) (2012) 10337–10345, https://doi.org/10.1016/j.ijhydene.2012.04.022.
[91] S. Taub, R.E.A. Williams, X. Wang, D.W. McComb, J.A. Kilner, A. Atkinson, Acta Mater. 81 (2014) 128–140, https://doi.org/10.1016/j.ssi.2015.09.024.
[92] C. Sındıraç, S. Çakırlar, A. Büyükaksoyc, S. Akkurt, Lowering the sintering temperature of solid oxide fuel cell electrolytes by infiltration, J. Eur. Ceram. Soc. 39 (2–3) (2019) 409–417, https://doi.org/10.1016/j.jeurceramsoc.2018.09.029.
[93] A.P. Grosvenor, M.C. Biesinger, R.S.C. Smart, N.S. McIntyre, New interpretations of XPS spectra of nickel metal and oxides, Surf. Sci. 600 (2006) 1771–1779, https://doi.org/10.1016/j.susc.2006.01.041.